



**HAL**  
open science

## Validation of a mathematical model of arterial wall mechanics with drug induced vasoconstriction against ex vivo measurements

Sara Costa Faya, Wesley Callan, Marina Vidrascu, Miguel Angel Fernández, Pieter-Jan Guns, Damiano Lombardi

### ► To cite this version:

Sara Costa Faya, Wesley Callan, Marina Vidrascu, Miguel Angel Fernández, Pieter-Jan Guns, et al.. Validation of a mathematical model of arterial wall mechanics with drug induced vasoconstriction against ex vivo measurements. 2024. hal-04597238v2

**HAL Id: hal-04597238**

**<https://inria.hal.science/hal-04597238v2>**

Preprint submitted on 19 Dec 2024

**HAL** is a multi-disciplinary open access archive for the deposit and dissemination of scientific research documents, whether they are published or not. The documents may come from teaching and research institutions in France or abroad, or from public or private research centers.

L'archive ouverte pluridisciplinaire **HAL**, est destinée au dépôt et à la diffusion de documents scientifiques de niveau recherche, publiés ou non, émanant des établissements d'enseignement et de recherche français ou étrangers, des laboratoires publics ou privés.



Distributed under a Creative Commons Attribution 4.0 International License

# Validation of a mathematical model of arterial wall mechanics with drug induced vasoconstriction against *ex vivo* measurements

Costa Faya Sara<sup>1\*</sup>, Wesley Callan<sup>2</sup>, Vidrascu Marina<sup>1</sup>,  
Fernández Miguel A.<sup>1</sup>, Guns Pieter-Jan<sup>2</sup>, Lombardi Damiano<sup>1</sup>

<sup>1\*</sup>Sorbonne Université & CNRS, UMR 7598 LJLL, 75005 Paris France –  
Inria, 75012 Paris, France.

<sup>2</sup>University of Antwerp, 2000 Antwerp, Belgium.

\*Corresponding author(s). E-mail(s): [sara.costa-faya@inria.fr](mailto:sara.costa-faya@inria.fr);  
Contributing authors: [callan.wesley@uantwerpen.be](mailto:callan.wesley@uantwerpen.be);  
[marina.vidrascu@inria.fr](mailto:marina.vidrascu@inria.fr); [miguel.fernandez@inria.fr](mailto:miguel.fernandez@inria.fr);  
[pieter-jan.guns@uantwerpen.be](mailto:pieter-jan.guns@uantwerpen.be); [damiano.lombardi@inria.fr](mailto:damiano.lombardi@inria.fr);

## Abstract

**Purpose:** In this work we investigate a mathematical model in order to reproduce experimental data of arterial compliance under the action of vasoconstrictors and vasodilators related to pharmacological studies.

**Methods:** The considered model is a 3D-shell with active fibers. Model parameters are identified by means of an optimization procedure.

**Results:** The resulting model was able to reproduce the experimental data and predict the system behavior in scenarios other than those used for the parameter estimation. This enables the assessment of different scenarios concerning the impact of the molecules on the active or passive contributions of the arterial wall.

**Conclusion:** The results suggest that smooth muscle cells contraction modulates stiffness through direct fiber-induced regulation of vascular tone, while parameters related to the passive arterial wall component remain relatively stable across different vasoactive scenarios.

**Keywords:** Mathematical modeling, Parameter estimation, Active fibers, 3D shell, Vascular smooth muscle cells, Validation against experimental data

# 1 Introduction

Arterial compliance, the capacity of the aorta to extend and recoil, is crucial for regulating cardiac output and maintaining blood flow in the systemic circulation [1]. Conversely, arterial stiffness, the inverse of compliance, is a predictor of cardiovascular health [2, 3]. Pulse wave velocity (PWV) serves as a non-invasive method to evaluate arterial stiffness in both human and animal subjects, indicating the speed of propagation of blood pressure waves [4, 5]. PWV measurement can provide a comprehensive assessment of arterial stiffness either globally, using applanation tonometry [6, 7], or locally, via ultrasound imaging [3, 8]. For additional techniques beyond applanation tonometry and ultrasound imaging, we refer to [9]. During aging, PWV increases due to arterial remodeling in response to prolonged hemodynamic stress, reflecting changes in the extracellular matrix such as the elastin: collagen ratio, which affects structural wall stiffness [2, 10].

Traditionally, arterial stiffness was attributed solely to the passive biomechanical properties of the aorta [11]. However, recent investigations have underscored the dynamic involvement of vascular smooth muscle cells (SMCs) and endothelial cells (ECs) in regulating arterial stiffness through modulation of vascular tone [12–14]. This active stiffness modulation, facilitated by adjustments in vascular tone, enables adaptation to acute hemodynamic stress through vasoconstriction by SMCs and release of vasoactive molecules by ECs [15]. While PWV is an independent predictor of cardiovascular health, it lacks the ability to provide detailed insights into passive or active modifications of arterial stiffness [11, 16]. To address this, arterial stiffness can be studied in dedicated *ex vivo* setups, offering the advantage of isolating passive stiffness and evaluating active modulation independent of *in vivo* factors, such as heart rate or blood pressure [10, 11, 16]. Previously, the Rodent Oscillatory Tension Setup for measuring Arterial Compliance (ROTSAC) effectively distinguished between active and passive contributions to arterial stiffness [11, 16]. Interestingly, it has been demonstrated that vasoconstrictors increased active stiffness at lower pressures while simultaneously reducing overall stiffness at higher pressures [16, 17].

The present work is aimed to develop a mathematical model capable of simulating the active contribution of SMCs to arterial stiffness. The objective of this work is twofold: firstly, the model is designed with the purpose of reproducing the available experimental data of the ROTSAc setup reported in [11]. Secondly, we aim to investigate how SMC contraction affects arterial stiffness through two mechanisms: direct fiber-induced regulation of vascular tone (*scenario I*) and, additionally, through indirect adjustment of intrinsic stiffness (reflected by Young’s modulus  $E$ ) (*scenario II*), and to what extent changes in geometry (i.e., diameter) are modulating biomechanical assessment. A specific question is also whether the *in silico* model can reflect the collagen unloading phenomena at elevated pressures previously reported in [16, 17].

We consider a simple modeling approach that captures the dynamics of vascular tone regulation, enabling the reproduction of experimental data and facilitating the comprehension of the mechanical behavior of arterial segments and the role of SMCs in arterial stiffness under different conditions. Furthermore, the use of a limited and manageable set of parameters facilitates the investigation of how SMC contraction contributes to arterial stiffness, particularly while investigating mechanical responses

such as vasoconstriction and vasodilation effects. The proposed mathematical model combines in parallel an hyperelastic 3D-shell model with a simplified active fiber description of the SMCs. In particular, an Ogden hyperelastic law is used for the passive component while the active effects rely on an affine stress-strain relationship.

Although structure-based passive mechanical models of blood vessels have been studied extensively [36–41], there remains a notable gap in the development of models addressing active properties. Mechanical studies of active vessels have predominantly relied on phenomenological models, primarily due to the complex micro-environment of SMCs and the coupled mechanical and chemical kinetics [42–44]. The majority of the active blood vessel constitutive models use uniaxial length-tension relationships in the circumferential direction as motivated by the circumferential arrangement of SMCs [21, 45–47].

In general, there is a lack of studies modeling SMC activation within the continuum mechanics framework. For example, in [44] a mechanochemical 3D continuum model for SMC contraction based on their one-dimensional model (see [48]). However, although the model has been developed in a 3D continuum framework, uniaxial examples have been shown only. In [19] a 3D-derived, fiber-reinforced, hyperelastic structural model, coupled with an axisymmetric, reduced-order model for blood flow is introduced. This model incorporates the relationship between vessel transmural pressure and lumen area via a Holzapfel–Ogden type law, while also considering residual stresses along the vessel’s thickness and length. Despite the increased complexity and parameter count compared to standard pressure-area tube laws, the advantages of employing such a model are numerous. Firstly, it can account for various conditions and pharmacological agent effects, such as axial loading, fiber dispersion, residual stress, and potentially active contractility. Secondly, the structural model developed by Holzapfel and colleagues that is used in [19] captures the nonlinear behavior of vascular tissue, especially under blood pressure loads significantly above the physiological range.

In the present work, the proposed 3D structural model shares certain features with existing 3D models but also introduces new contributions. Our model integrates a 3D hyperelastic law for the passive component, strengthened by active fibers. Unlike the approaches of [19] or of [44], we have not included the chemical driving mechanism. However, we have employed 3D-shell formulation to avoid numerical locking and manage large displacements, as evidenced in dynamic simulations. In contrast to [19], which performs the model validation through isometric tests, our model is validated as well through uniaxial static tests with biaxial deformation measurements and uniaxial dynamical ones. In general, with this type of models we could incorporate them in *in vivo* more complex geometries and be able to describe a full hemodynamic model.

The paper is organized as follows. Section 2 provides details on the experimental setup and discusses the available data for the simulations. It also presents the mathematical model used to simulate the arterial wall with active behavior. Section 3 showcases some numerical results. Finally, the conclusions together with some perspectives are drawn in Section 4.

## 2 Methods

In this section, the experimental methods and the collected data that have been employed for the numerical simulations are presented. It also provides an overview of the structural model that has been used to reproduce the experimental data and to give some insight of the fore-mentioned scenarios. Finally, this section introduces the methodology employed for parameter estimation and model validation.

### 2.1 Experimental data

**Evaluation of vascular reactivity.** For the evaluation of vascular reactivity, aortic segments were set at a preload of 20 mN to achieve a loading equivalent to blood pressure of 100 mmHg. SMC contraction was assessed by incremental concentrations of phenylephrine (PE; ranging from 3 nM to 3  $\mu$ M), an  $\alpha$ 1-adrenergic receptor agonist. Furthermore, exogenous nitric oxide donor, 2-(N,N-diethylamino)-diazolot-2-oxide sodium salt hydrate (DEANO; ranging from 0.03 nM to 10  $\mu$ M) was administered to evaluate passive (intrinsic) stiffness in the absence of SMC contraction/contribution.

***Ex vivo* stiffness.** The *ex vivo* stiffness of aortic segments was assessed using the Rodent Oscillatory Setup to study Arterial Compliance (ROTSAC), as detailed by Leloup et al. [11] (see Figure 1(left)). Briefly, 2 mm aortic segments were placed between two parallel hooks within 10 mL organ baths. These segments were submerged in Krebs-Ringer (KR) solution maintained at 37 °C, with a gas mixture of 95% O<sub>2</sub> and 5% CO<sub>2</sub>, and pH adjusted to 7.4. The composition of the Krebs-Ringer solution comprised NaCl 118 mM, KCl 4.7 mM, CaCl<sub>2</sub> 2.5 mM, KH<sub>2</sub>PO<sub>4</sub> 1.2 mM, MgSO<sub>4</sub> 1.2 mM, NaHCO<sub>3</sub> 25 mM, CaEDTA 0.025 mM, and glucose 11.1 mM. Force and displacement of the upper hook were controlled and recorded using a force length transducer. Aortic segments underwent cyclic stretching between alternating preloads, mimicking “diastolic” and “systolic” transmural pressures at a frequency of 10 Hz, corresponding to the physiological heart rate in mice (600 beats per minute). Transmural pressure was determined using the Laplace relationship. Aortic extension was calibrated through optical camera imaging, capturing pictures at different stretches to calibrate the upper hook and allowing calculation of vessel diameters during systole and diastole. Subsequently, the Peterson modulus of elasticity,  $E_p$ , was computed at various pressure levels.  $E_p$  was calculated using the expression:

$$E_p = D_0 \frac{\Delta P}{\Delta D},$$

where  $\Delta P$  represents the difference in pressure (maintained constant at 40 mmHg),  $D_0$  denotes the “diastolic” diameter, and  $\Delta D$  indicates the change in diameter between “diastolic” and “systolic” pressure. The protocol encompassed the assessment of arterial stiffness ( $E_p$ ) at different pressures, ranging from 60 – 100 mmHg up to 120 – 160 mmHg, with incremental intervals of 20 mmHg. The pressure-stiffness relationship was evaluated under physiological conditions (using Krebs-Ringer solution), in a maximally-contracted state (induced by 2  $\mu$ M PE, reflecting active components), and in the absence of active stiffness (utilizing 2  $\mu$ M of DEANO, a nitric oxide donor to negate any contribution of SMC contraction).

## 2.2 Mathematical modeling

Arteries form an anisotropic structure composed of three primary layers (for more details, please refer to Ref. [18]): the adventitia, situated on the outermost part, contains collagen fibers and acts as a protective covering for the artery; below the adventitia lies the media layer, housing SMCs that are responsible for vascular tone regulation; and the innermost intima, lined with ECs, serves as a protective barrier between the bloodstream and arterial wall.

In the present work, the arterial wall is modeled as a passive hyperelastic material using a 3D-shell model. Shell models are particularly useful in cardiovascular simulations when the thickness-to-size ratio of the solid structure is small, as is the case for the arterial wall. Specifically, 3D-shell models employ a quadratic kinematic assumption on displacements, making them well-suited for capturing the large deformations of the arterial wall during experiments. These models provide notable advantages, such as enabling the application of general 3D constitutive relations within the shell context and accurately capturing through-thickness stress variations. For a comprehensive overview of shell models, please refer to [28, 29].

Additionally, a layer of fibers is included to describe the SMCs induced vasoconstriction and vasodilation phenomena. Since the focus is primarily on the media layer, the fibers are aligned with the circumferential direction [19–22]. The anisotropic behavior of the passive matrix due to collagen fibers is neglected.

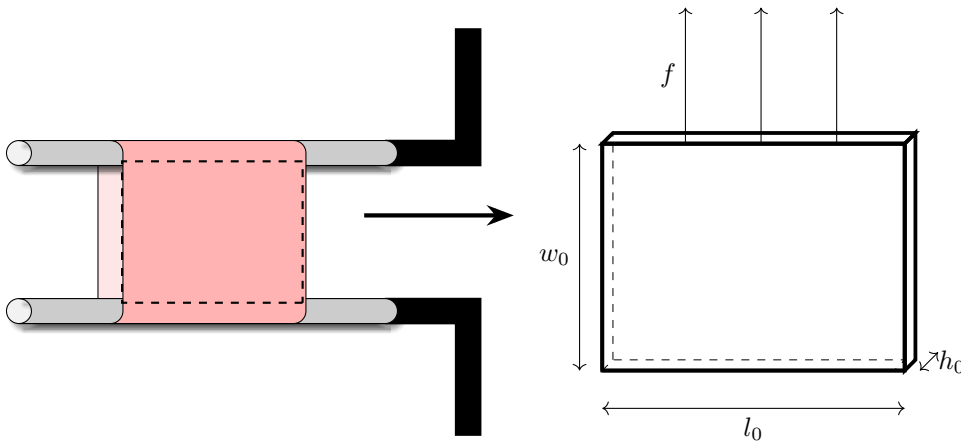


**Fig. 1:** Schematics of the ROTSAC setup (left) and simplified geometry considered in the mathematical model (right)

Owing to the symmetry of the ROTSAC setup (Figure 1(left)), a simplified geometrical configuration has been considered in the mathematical model. It consists of one of the lateral sides of the tissue mounted on the hooks, as presented in Figure 1(right), which is here assumed to be flat in the stress-free configuration.

### 2.2.1 3D-shell model

Let  $\Omega \subset \mathbb{R}^3$  denote the reference (stress-free) configuration of the tissue segment. The boundary of  $\partial\Omega$  is partitioned into three subsets:  $\Gamma_N$ , which corresponds to the upper boundary of the domain where the force is applied to stretch the tissue;  $\Gamma_D$ , representing the part of the aortic segment attached to the lower hook, which is clamped during the whole experiment; and  $\Gamma_L$ , that are the lateral boundaries of the aortic segment. We denote by  $\mathbf{n}$  the outward unit normal on the boundary  $\Gamma_N$ . The reference configuration  $\Omega$  is characterized by  $l_0$ ,  $w_0$  and  $h_0$ , that are the stress-free length, width and thickness, respectively, as shown in Figures 1(right) and 2.

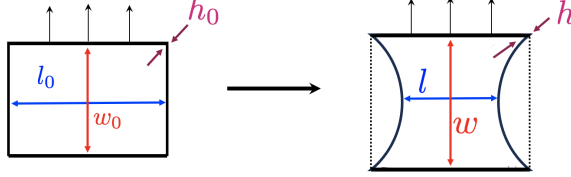


**Fig. 2:** Geometrical configuration of the shell. On the left the reference configuration and on the right the deformed one

The deformation of the continuum medium is given as the map  $\varphi : \Omega \times [0, T] \mapsto \mathbb{R}^3$ . The deformation gradient  $\mathbf{F}$ , is expressed as  $\mathbf{F}(\mathbf{x}, t) = \nabla_{\mathbf{x}}\varphi(\mathbf{x}, t)$ , and its determinant  $J$ , as  $J(\mathbf{x}, t) = \det(\mathbf{F}(\mathbf{x}, t))$ . The displacement field  $\mathbf{d}$  is defined as  $\mathbf{d}(\mathbf{x}, t) = \varphi(\mathbf{x}, t) - \mathbf{x}$ .

The equilibrium of the system is given by the following nonlinear elastodynamics boundary value problem:

$$\begin{cases} \rho \partial_{tt} \mathbf{d} - \operatorname{div}(\mathbf{F}(\mathbf{d})\boldsymbol{\Sigma}(\mathbf{d})) = \mathbf{0}, & \text{in } \Omega, \\ \mathbf{F}(\mathbf{d})\boldsymbol{\Sigma}(\mathbf{d})\mathbf{n} = \mathbf{f}_s, & \text{on } \Gamma_N, \\ \mathbf{d} = \mathbf{0}, & \text{on } \Gamma_D, \end{cases} \quad (1)$$

where  $\rho$  stands for the density of the tissue,  $\mathbf{f}_s$  represents the time-dependent volume force and  $\boldsymbol{\Sigma}(\mathbf{d})$  is the second Piola-Kirchhoff stress tensor of the tissue.

The active SMC fibers are assumed to be perfectly attached to the solid so that to model the active behavior of the artery wall, an active-stress formalism [23] is chosen, which consists in adding an active component to the passive stress tensor [24], viz.,

$$\boldsymbol{\Sigma}(\mathbf{d}) = \boldsymbol{\Sigma}_p(\mathbf{d}) + \boldsymbol{\Sigma}_a(\mathbf{d}),$$

with  $\boldsymbol{\Sigma}_a(\mathbf{d})$  and  $\boldsymbol{\Sigma}_p(\mathbf{d})$  respectively denoting the active and passive components of the stress.

An Ogden hyperelastic constitutive law is chosen to describe the homogeneous and isotropic passive component, since it accommodates large deformations and nonlinear material responses, providing a more accurate representation for the behavior of

complex materials like biological tissue [25, 26]. We hence have

$$\boldsymbol{\Sigma}_p = 2 \frac{\partial W}{\partial \mathbf{C}},$$

where  $\mathbf{C} := \mathbf{F}^T \mathbf{F}$  stands for the right Cauchy-Green deformation tensor and the strain energy density function  $W$  given by the relation [27]:

$$W = c_1(I_1 - 3) + c_2(I_2 - 3) + a(I_3 - 1) - (c_1 + 2c_2 + a)\ln(I_3), \quad (2)$$

in terms of the invariants of  $\mathbf{C}$ , namely,  $I_1 = \text{tr}(\mathbf{C})$ ,  $I_2 = \frac{1}{2}(I_1^2 - \mathbf{C}:\mathbf{C})$ , and  $I_3 = \det(\mathbf{C}) = J^2$ .

In (2), the constants  $c_1, c_2$  and  $a$  stand for the material parameters, that can be expressed as a function of the Young modulus,  $E$ , and the Poisson ratio,  $\nu$ , as follows (see Appendix B):

$$\begin{cases} c_1 = \frac{E}{4(1+\nu)(1+\frac{1}{\kappa})}, \\ c_2 = \frac{c_1}{\kappa}, \\ a = \frac{\nu E}{4(1+\nu)(1-2\nu)} - \frac{c_1}{\kappa}, \end{cases}$$

where usually  $c_2$  can be chosen such that  $c_2 = c_1/\kappa$ , with  $\kappa \in [2, 100]$ .

The elastodynamics equations (1) can be reformulated in weak variational form as follows

$$\left\{ \begin{array}{l} \text{Find } \mathbf{d} \in \mathbf{V} \text{ such that} \\ \int_{\Omega} \rho \partial_{tt} \mathbf{d} \cdot \mathbf{v} + \int_{\Omega} \boldsymbol{\Sigma}(\mathbf{d}) : \delta_{\mathbf{d}} \mathbf{E}(\mathbf{d}) \mathbf{v} = \int_{\Gamma_N} \mathbf{f}_s \cdot \mathbf{v}, \quad \forall \mathbf{v} \in \mathbf{V}, \end{array} \right. \quad (3)$$

where  $\mathbf{E}(\mathbf{d}) := \frac{1}{2}(\mathbf{C} - \mathbf{I})$  is the Green-Lagrange strain tensor and  $\delta_{\mathbf{d}} \mathbf{E}(\mathbf{d}) \mathbf{v}$  stands for the differential of  $\mathbf{E}$  in the direction  $\mathbf{v}$ .

A fundamental drawback of the full 3D model (3) is that, due to the thin-walled nature of  $\Omega$ , 3D finite element approximations of (3) suffer from artificial stiffening phenomena, known as numerical locking (see, e.g., [28]), which often requires highly refined meshes across the thickness and can hence become computationally expensive in practice. These issues are traditionally avoided by considering reduced models based on shell theory in combination with an appropriate treatment of numerical locking at the discrete level (see, e.g., [28, 29]). In this work, we consider a 3D-shell modeling approach based on a quadratic kinematic behavior along the transverse coordinate (see [30]), without any plane stress assumption. This enables the use of general constitutive laws. The basic idea consists in replacing, in (3), the original full 3D space  $\mathbf{V}$  by the following reduced space:

$$\mathbf{V}^{\text{sh}} := \left\{ \mathbf{v} \in \mathbf{V} : \mathbf{v} = \mathbf{v}_0 + \mathbf{v}_1 \xi^3 + \mathbf{v}_2 (\xi^3)^2, \quad \mathbf{v}_i \in [H^1(\mathcal{S})]^3, \quad i = 0, 1, 2 \right\}, \quad (4)$$



where  $\xi^3$  corresponds to the local transverse coordinate of  $\Omega$  and  $\mathcal{S}$  to the mid-surface of  $\Omega$ . The resulting 3D-shell model hence reads as follows:

$$\begin{cases} \text{Find } \mathbf{d} \in \mathbf{V}^{\text{sh}} \text{ such that} \\ \int_{\Omega} \rho \partial_{tt} \mathbf{d} \cdot \mathbf{v} + \int_{\Omega} \boldsymbol{\Sigma}(\mathbf{d}) : \delta_{\mathbf{d}} \mathbf{E}(\mathbf{d}) \mathbf{v} = \int_{\Gamma_N} \mathbf{f}_s \cdot \mathbf{v}, \quad \forall \mathbf{v} \in \mathbf{V}^{\text{sh}}. \end{cases} \quad (5)$$

The numerical approximation of (5) is performed via the finite element method, in which the space  $\mathbf{V}^{\text{sh}}$  is replaced by the discrete space  $\mathbf{V}_H^{\text{sh}}$  spanned by quadratic displacements across the thickness and affine on each section [28, 30, 31]. This yields a  $\mathbb{P}_1 \otimes \mathbb{P}_2$  prismatic element with 9 nodes (see Figure 3). Numerical locking is avoided using a MITC (Mixed Interpolated Tensorial Components) approach which guarantees robustness with respect to the thickness parameter (see, e.g., [28]).

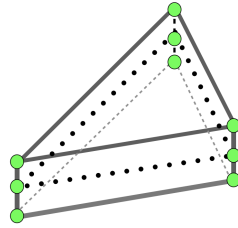


**Fig. 3:**  $\mathbb{P}_1 \otimes \mathbb{P}_2$  3D-shell element

All the simulations presented in this work have been performed using FELiScE<sup>2</sup>.

### 2.2.2 Active fiber model

The main hypotheses regarding the fibers are the following:

- The fibers are part of the shell and are distributed through the thickness in the circumferential direction;
- There is no sliding between the fibers and the shell;
- The fibers are characterized by an affine stress-strain constitutive law.

Here, we consider the active fibers model proposed in Ref. [32], so that

$$\boldsymbol{\Sigma}_a := (k_0 + k_1 e_{\mathbf{ff}}) \mathbf{f} \otimes \mathbf{f}, \quad (6)$$

where  $k_0$  denotes the pre-stress of the fiber,  $k_1$  is the elastic modulus,  $e_{\mathbf{ff}}$  is the fiber deformation and  $\mathbf{f}$  is the unitary tangent vector to the fiber direction. The deformation along the fiber directions is given by the relation  $e_{\mathbf{ff}} := \mathbf{f}^T \mathbf{E} \mathbf{f}$ , where  $\mathbf{E}$  is the Green-Lagrange strain tensor defined above.

<sup>2</sup><https://gitlab.inria.fr/felisce>

### 2.3 Parameter estimation and model validation

The mathematical model (3), together with the hyperelastic law (2) and the fibers constitutive law (6), contains a set of parameters (Young modulus,  $E$ ; active pre-stress,  $k_0$ , and elastic modulus,  $k_1$ , of the fibers;  $\kappa$ , that stems from the Ogden's law; initial length,  $l_0$ , width,  $w_0$ , and thickness,  $h_0$ , of the aortic segment<sup>3</sup>) that are unknown and are determined through a parameter estimation procedure. After spatial and temporal discretization, the model (3), with (2) and (6), yield the nonlinear system

$$F(\mathbf{f}_s, \boldsymbol{\theta}; \mathbf{Y}) = 0, \quad (7)$$

where  $\mathbf{f}_s$  is the given force, that can be measured,  $\boldsymbol{\theta} = (E, k_0, k_1, \kappa; l_0, w_0, h_0)$  are the model parameters and  $\mathbf{Y}$  is the model output, that corresponds to the displacement degrees of freedom. The inputs of the model are  $\boldsymbol{\theta}$  and  $\mathbf{f}_s$ .

The purpose of the parameter estimation is evaluating some unknown inputs of the model such that the outputs match the experimental measurements. The parameter estimation problem can be formulated as follows: given the force  $\mathbf{f}_s$ , the discrete model (7) and the experimental data, find the parameters  $\boldsymbol{\theta}$  that minimize the discrepancy between the simulated model predictions and measurements. Mathematically, this problem can be formulated as the optimization problem

$$\min_{\substack{\boldsymbol{\theta} \in \mathbf{W} \\ F(\mathbf{f}_s, \boldsymbol{\theta}, \mathbf{Y})=0}} J(\mathbf{Y}), \quad (8)$$

where  $J : \mathbb{R}^n \rightarrow \mathbb{R}$  is given cost function (viz., discrepancy between simulation and measurements) and  $\mathbf{W} \subset \mathbb{R}^n$  stands for the set of admissible parameters. In this paper, problem (8) is solved via a Control Random Search (CRS) optimization algorithm (see Appendix D).

Initially, the estimation is done for each aortic segment under Krebs-Ringer solution. Subsequently, estimations are conducted following the administration of a vasoactive drug, either a vasoconstrictor or vasodilator. The results of the parameter estimation provides hence insight on whether the compound solely impacts SMCs (scenario I) or additionally introduces additional intrinsic stiffness (scenario II). Specifically, if only the fiber parameters from the active contribution, such as  $k_0$  and  $k_1$ , are affected, it suggests that the first scenario is the most plausible one. However, if the Young's modulus also needs modification, then the compound is likely to introduce stiffness (scenario II). To establish a range for the active pre-stress parameter, data from isometric experiments have been used.

To solve the optimization problem (8), a CRS2 with local mutation optimization algorithm [33] (for more details, see Appendix D) that is implemented in the NLOpt (nonlinear optimization) package by Johnson [34] has been employed.

---

<sup>3</sup>All the segments have an approximated length of 2 mm and width of 1 mm. However, there might be slight differences between them and the initial configuration needs thus to be estimated.

### 2.3.1 Parameter estimation in baseline conditions

During the ROTSAC static calibration, the experimental measurements are the length ( $l_m$ ) and the width ( $w_m$ ) of the aortic segments for some given forces  $\mathbf{f}_s$  while when the segments are dynamically stretched, the measured data is the width ( $\tilde{w}_m$ ). In this case, the cost function of the parameter estimation problem (8) has the following form

$$J_1(\mathbf{Y}) = \sqrt{\frac{1}{k} \sum_{i=1}^k \left| l^{(i)}(\mathbf{Y}) - l_m^{(i)} \right|^2 + \left| w^{(i)}(\mathbf{Y}) - w_m^{(i)} \right|^2} + \sqrt{\frac{1}{n} \sum_{i=1}^n \left| \tilde{w}^{(i)}(\mathbf{Y}) - \tilde{w}_m^{(i)} \right|^2}. \quad (9)$$

Here,  $l_m^{(i)}$  and  $w_m^{(i)}$  represent the measured length and width, respectively, during static experimental calibration, with  $i = 1, \dots, k$  denoting the number of measurements.  $\tilde{w}_m^{(i)}$  denotes the measured width during oscillation, with  $i = 1, \dots, n$  indicating the number of measurements.  $l^{(i)}(\mathbf{Y})$  and  $w^{(i)}(\mathbf{Y})$  represent the predicted values of length and width, respectively, during static experimental calibration, while  $\tilde{w}^{(i)}(\mathbf{Y})$  denotes the predicted value of width during the oscillation.

### 2.3.2 Parameter estimation in the presence of vasoactive substances

**Determination of the range of the pre-stress.** The isometric experiments provide data that show the force exerted by the vessel in response to a specific vasoconstrictor (or vasodilator) dosage within a static setup. The relevance of these experiments, is that they can provide an estimation of the range of the value of the active pre-stress at each drug concentration  $C$ , with  $C$  being either  $C^{\text{PE}}$ , the PE concentration, or  $C^{\text{DEANO}}$ , the DEANO concentration. In particular, the ROTSAC measurements were taken at  $C = 2 \mu\text{M}$  and the isometric data allow the estimation of the range of the value of  $k_0$  at the specified  $C$ .

We consider that the total measured force is

$$F_m = \beta + F_1, \quad (10)$$

where  $\beta$  is the force at zero concentration and  $F_1$  is the isometric force felt by the upper hook in the presence of a vasoactive substance. Assume that the relation between  $F_1$  and the active pre-stress,  $k_0$ , is linear and can be expressed as  $F_1 = \alpha k_0$ . The mathematical model (3)–(6), has been used applying homogeneous Dirichlet boundary conditions on the upper and on the lower boundary of the domain  $\Omega$  to estimate  $\alpha$ . Substituting the expression for  $F_1$  in (10),  $F_m = \beta + \alpha k_0$ .

Using the following tension-dose relationship [35], the active pre-stress results

$$k_0(C; m, EC_{50}) = S_{\max}^{\text{PE}} \frac{[C^{\text{PE}}]^m}{[C^{\text{PE}}]^m + EC_{50}^m} - S_{\max}^{\text{DEANO}} \frac{[C^{\text{DEANO}}]^m}{[C^{\text{DEANO}}]^m + EC_{50}^m}, \quad (11)$$

where  $S_{\max}^{\text{PE}}$  is the maximal tension for PE (saturation level),  $S_{\max}^{\text{DEANO}}$  is the maximal tension for DEANO,  $m$  is the slope parameter and  $EC_{50}$  the concentration at which 50% of maximal force is obtained.

Finally, the expression of the total measured force is

$$F_m = \beta + \alpha \left( S_{\max}^{\text{PE}} \frac{[C^{\text{PE}}]^m}{[C^{\text{PE}}]^m + EC_{50}^m} - S_{\max}^{\text{DEANO}} \frac{[C^{\text{DEANO}}]^m}{[C^{\text{DEANO}}]^m + EC_{50}^m} \right). \quad (12)$$

During the isometric experiments, the aortic segments have been preloaded with a force  $\beta = 20$  mN in the absence of drugs ( $C^{\text{PE}} = C^{\text{DEANO}} = 0$ ) and also  $S_{\max}^{\text{PE}}$  and  $S_{\max}^{\text{DEANO}}$  are known. By employing the previous  $F_m$  - dose relation, a fitting of the measured forces to equation (12) to estimate the values of  $m$  and  $EC_{50}$  was performed. After fitting the measured force for several concentrations in the set of aortic segments, it is possible to determine the range of  $k_0$  for a vasodilator or for a vasoconstrictor.

From equation (11), it can be remarked that when there is only PE in the organ bath,  $C^{\text{DEANO}} = 0$  and the second term vanishes. After DEANO has been added on the bath,  $C^{\text{PE}}$  is equal to the concentration at saturation, so  $C^{\text{PE}} = 3 \mu\text{M}$ .

**Dynamic oscillation.** In the context of ROTSAC dynamic oscillation with vasoconstrictors/vasodilators, two scenarios are tested. In the first one, only the active fiber parameters  $k_0$  and  $k_1$  are subject to estimation, while  $E$ ,  $l_0$ ,  $w_0$ , and  $h_0$  remain fixed based on the corresponding segment in Krebs-Ringer solution. Conversely, in the second scenario, parameters  $E$ ,  $k_0$ ,  $k_1$ , and  $h_0$  are open to estimation, with  $l_0$  and  $w_0$  held constant. The key distinction lies in allowing  $E$  to vary during estimation for the second scenario, whereas only the active fiber parameters are adjusted in the first one. Here the parameter estimation is done when a vasoconstrictor (PE) or a vasodilator (DEANO) are added to the Krebs-Ringer solution to assess the effects. The available experimental measurements are the values of width ( $\tilde{w}_m$ ) of the aortic segment dynamically stretched at 80-120 mmHg. Under the effect of a drug, the cost function of the minimization problem (8) is

$$J_2(\mathbf{Y}) = \sqrt{\frac{1}{n} \sum_{i=1}^n \left| \tilde{w}^{(i)}(\mathbf{Y}) - \tilde{w}_m^{(i)} \right|^2}, \quad (13)$$

where  $\tilde{w}_m^{(i)}$  is the measured experimental value of the width and  $\tilde{w}^{(i)}(\mathbf{Y})$  is the predicted value of the width at each point  $i = 1, \dots, n$  during the oscillation. Since there are no static experimental calibration data with drugs, there is no information of the length in the case of a vasoactive substance on the organ bath. The changes in the fiber parameters  $k_0, k_1$  and in  $E, h_0$ , will help to assess the fore-mentioned scenarios.

### 3 Numerical results

First, the results obtained from the parameter estimation of the model are presented. Next, numerical simulation (in baseline conditions and in the presence of vasoactive compounds) is performed. While various vasoconstrictors have been employed, the outcomes are primarily focused on PE due to its resemblance to the others. Finally, the behavior of the aortic segments under varying pressure conditions is explored.

### 3.1 Static experimental calibration

The static experimental calibration measurements of the length and width at different preloads (10, 20, 30, 40 and 50 mN) were considered for estimating the parameters  $\theta$  of each aortic segment in the baseline case (Krebs-Ringer solution), together with the dynamic data at 80 - 120 mmHg (using the cost function (9) with  $k = 5$  and  $n = 80$ ). The static part of results for the set of fifteen aortic segments considered in this studio are shown in Figure 4.

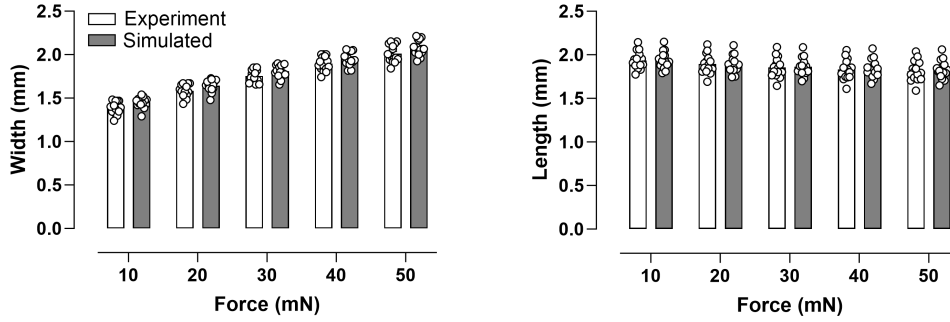


Fig. 4: Comparison between experimental and simulated static experimental calibrations

The comparison presented in Figure 4 shows that the simulated values for both width and length generally align with the experimental data across all force levels.

### 3.2 Simulation in the presence of vasoactive substances

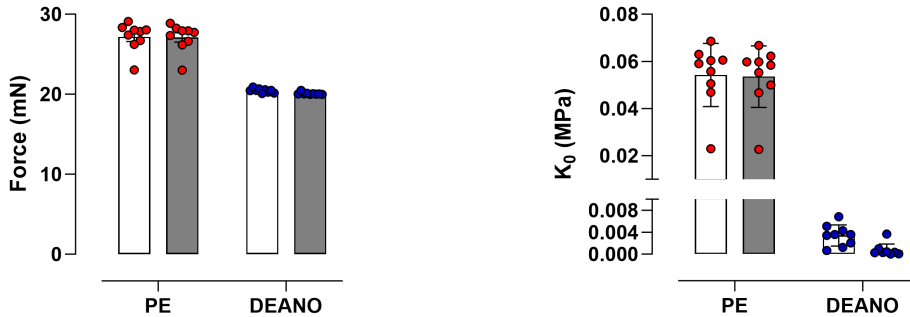


Fig. 5: Isometric force  $F_m$  at  $C = 2 \mu\text{M}$  (left); pre-stress at  $C = 2 \mu\text{M}$  (right)

**Estimation of the range of the pre-stress from the isometric data.** First, throughout the isometric tests, where a second set of nine aortic segments was considered, the average relative mean squared error (RMSE) between the experimental

and simulated data across all fittings of the isometric force (12) in the presence of PE ( $2 \mu\text{M}$ ) is  $0.56\% \pm 0.38\%$ , while  $1.86\% \pm 0.63\%$  for DEANO, ( $2 \mu\text{M}$ ) (see the fittings in Figure C1 in Appendix C). The results at  $C = 2 \mu\text{M}$  – the concentration at which dynamic measurements were taken – are shown in Figure 5. Upon examination of the values of the pre-stress,  $k_0$ , for the available set of aortic segments at a concentration of  $C = 2 \mu\text{M}$ , the range of  $k_0$  for PE and DEANO can be identified (see Figure 5). The observed range of  $k_0$  was  $[0.023, 0.067]$  MPa for PE and  $[-0.00014, 0.0043]$  MPa for DEANO. The fitting for all the concentrations is presented in Figure C2 in Appendix C.

**Simulation of ROTSAC dynamic oscillation data.** Next, parameters were estimated and numerical simulations of experimental data were conducted across 15 segments using a Krebs-Ringer solution (using the cost function (9)). From the set of all segments, Table 1 details the estimated parameters for one aortic segment (seg #1) under baseline, contracted, and dilated conditions, with corresponding experimental and simulated datasets shown in Figures 6A and 6B. Figure 6 illustrates the impact of vasoconstrictors and vasodilators on arterial behavior (with the parameter estimation performed using the cost function (13) with  $n = 80$ ). Particularly, Figure 6C displays the Peterson modulus derived from experimental and simulated data under KR, PE, and DEANO conditions, while aortic segments underwent oscillations within the pressure range of 80 - 120 mmHg. This graphical representation highlights differences in stiffness across these conditions, with PE exhibiting heightened stiffness relative to baseline, and DEANO resulting in comparable stiffness to baseline. Such observations underscore the model’s adeptness in capturing the vascular system’s mechanical responses to various vasoactive agents.

Parameter	KR	PE	DEANO
$E$ (MPa)	0.13248	0.13248	0.12717
$k_0$ (MPa)	$6.4 \cdot 10^{-6}$	0.01	$-1.348 \cdot 10^{-4}$
$k_1$ (MPa)	0.191	0.457	0.188
$l_0$ (mm) = 1.97 $w_0$ (mm) = 0.13 $h_0$ ( $\mu\text{m}$ ) = 53			

**Table 1:** Parameters and stress-free configuration for KR, PE, and DEANO for seg #1 in scenario II for PE and DEANO

Correlation plots (Figures 6D, 6E, 6F) were generated to measure the concordance between simulated and experimental data across different conditions. A statistical covariance matrix  $Q \in \mathbb{R}^{2 \times N}$  was computed to quantify variability and correlation, with  $N \in \mathbb{N}$  representing the number of points. From  $Q$ , a matrix  $C = \frac{1}{N-1} Q Q^T \in \mathbb{R}^{2 \times 2}$  was derived to reveal the shape and orientation of ellipses. The eigenvectors of  $C$  represent the principal axes of the ellipse and the square root of its eigenvalues will determine the ellipse’s width and height, with one of them reflecting the average difference between simulated and experimental data (RMSE) and another one giving an idea of the standard deviation of the fits. Overall, the correlation plots demonstrate a

consistent match between the simulated and experimental data, indicating the model's capability in capturing the SMCs behavior under KR, PE, and DEANO.

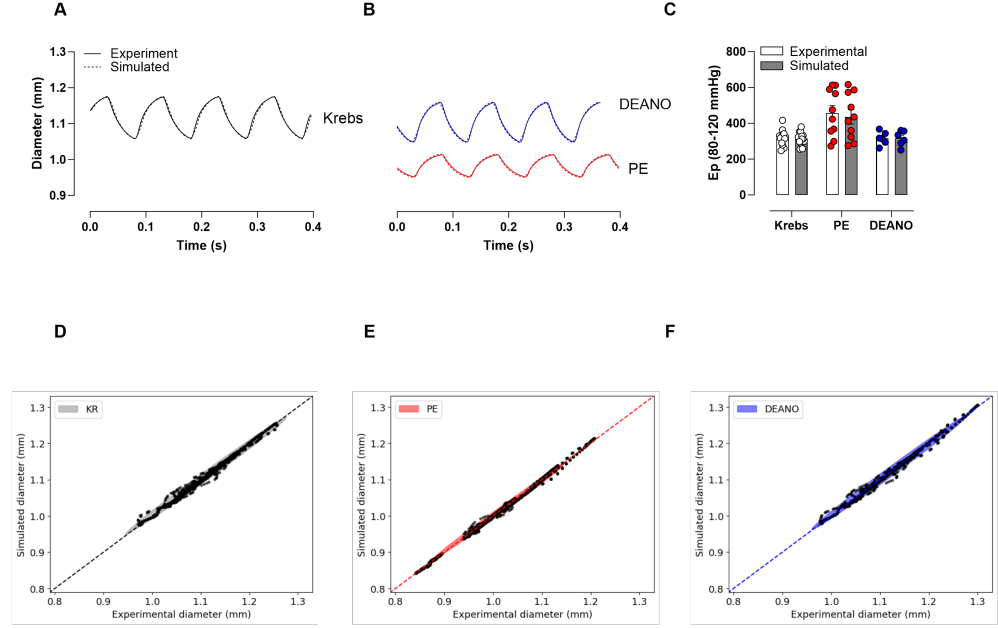


**Fig. 6:** Analysis of the impact of PE and DEANO when the segments are dynamically stretched at 80 - 120 mmHg. Time evolution of the experimental and simulated diameters of seg #1 (A, B); Peterson modulus (C); Correlation between experimental and simulated diameters (D, E, F). The ellipse intersects the unity line, which depicts where the simulated and experimental data would coincide perfectly, being the center of the ellipse the average position of the points

**Assessing the role of SMCs.** Finally, comparisons between the changes of fiber parameters ( $k_0$  and  $k_1$ ) in the presence of a vasoconstrictor or vasodilator with  $E$  and  $h_0$  constant (scenario I) or with re-estimation of  $E$  and  $h_0$  (scenario II) were investigated. The analysis depicted in Table 2 illustrates the effectiveness of integrating  $k_0$  and  $k_1$  under constant  $E$  and  $h_0$  conditions to fit dynamical experimental data within the pressure range of 80 - 120 mmHg.

KR (%)	Scn1 PE (%)	Scn2 PE (%)	Scn1 DEANO (%)	Scn2 DEANO (%)
0.60	1.60	0.44	0.63	0.58

**Table 2:** Average of the RMSE of the dynamic fittings for Krebs-Ringer and in both scenarios (Scn1 or Scn2) at 80 - 120 mmHg

The mean RMSE values for the dynamic fittings are all below 2%, indicating that both scenarios provide accurate representations of the compound’s effects on SMCs. Although the second scenario may yield a slightly better fit, the error in the first scenario is sufficiently low with just fiber parameter adjustments, suggesting that modifying the Young’s modulus is generally unnecessary. However, in cases where the error is larger, it may indicate that the compound also affects the intrinsic stiffness of the vessel, necessitating adjustments to parameters such as the Young modulus or thickness. Overall, the results suggest that the change of  $k_0$  and  $k_1$  in the presence of a vasoconstrictor or vasodilator with  $E$  and  $h_0$  constant, is generally sufficient, but there might be cases where improvements can be made by re-estimating  $E$  and  $h_0$ .

The active fiber parameters were changed in the presence of a vasoconstrictor with respect to the baseline (Figures 7A and 7B). The pre-stress is also seen to increase with the introduction of a vasoconstrictor (Figure 7A,  $p < 0.01$ ). The active elastic modulus experienced an increase (Figure 7B,  $p < 0.01$ ), indicating an augmentation in vessel stiffness. No differences were reported in the change in Young modulus following constriction with PE (Figure 7C). Overall, the majority of segments underwent a Young modulus change within the range of  $[-1, 1]$  %. While some cases exhibited a slightly larger deviation, on the whole, the scenario in which the change of fiber parameters ( $k_0$  and  $k_1$ ) in the presence of a vasoconstrictor or vasodilator with  $E$  and  $h_0$  constant appears to be a plausible one. No changes in aortic thickness were reported following PE stimulation (Figure 7D).

For simplicity, the results for DEANO were excluded from the graphs as they closely resemble those of KR. However, the response to DEANO is more complex to interpret, where the pre-stress may either rise or fall relative to the baseline. It’s important to acknowledge that DEANO was administered alongside the vasoconstrictor in the organ bath, making it challenging to isolate its specific effect. Among vasodilators, changes in pre-stress exhibit diverse patterns—sometimes increasing, other times decreasing. Vasodilators typically lower blood pressure and wall tension by dilating vessels and enhancing compliance, resulting in an overall reduction in pre-stress. However, the complex interaction of compensatory mechanisms and individual variations can influence the effect on pre-stress. On the other hand, with the other parameters ( $k_1$ ,  $E$  and  $h_0$ ) the obtained results are very close to the ones of KR.

**Evaluating the model in different pressure ranges.** After presenting the estimated parameters for each scenario, additional model validation was conducted by examining the predictability across different pressure ranges. The outcomes corresponding to the segment with parameters outlined in Table 1 (seg #1) are illustrated in Figure 8. The oscillations were represented only for KR and PE since the ones for DEANO are very similar to the ones of KR.

When aortic segments were stretched in Krebs-Ringer solution, the original estimated parameters were able to reproduce the data both in the ranges of 60 - 100 mmHg to 100 - 140 mmHg. However, there was an underestimation at higher pressures (120 - 160 mmHg). One possible explanation could be because the segments exhibited plasticity and did not recover the reference configuration ( $l_0$ ,  $w_0$  and  $h_0$ ) instantaneously. Consequently, it was necessary to take into account that the reference configuration had changed after large forces were applied. Then, a re-estimation of  $l_0$ ,  $w_0$  and  $h_0$



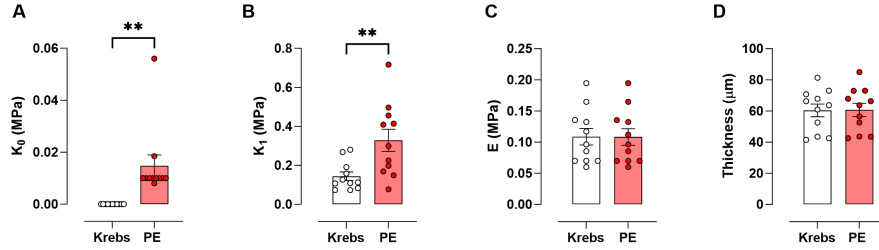


**Fig. 7:** Vessel parameters under different conditions. Change of the pre-stress (A), fibers elastic modulus (B), Young modulus (C) and thickness (D) for PE with respect to the baseline. The values for a vasodilator (DEANO) are omitted since they are very similar to the ones of KR

was needed for the pressure range 120 - 160 mmHg, while the rest of the parameters ( $E$ ,  $k_0$  and  $k_1$ ) were kept constant. After PE was added to the Krebs-Ringer solution, the change of the reference configuration was observed in all the pressure ranges so, again, the re-estimation of the initial length, width, and thickness was necessary. Finally, once DEANO was added to the organ bath, a similar behavior was observed, so the re-estimation was only needed for the highest pressure range.

From a biological perspective, the underestimation at higher pressures can be attributed to the properties of the arterial wall. When subjected to elevated forces, such as those experienced at higher pressure ranges, arterial segments may encounter layers of collagen within their structure. This discrepancy is particularly pronounced in KR solution, where the arterial segments experience greater pressure-induced deformation. Conversely, when PE is added, the effects are mitigated to some extent. This is because PE-induced constriction leads to smaller diameter arteries, reducing the likelihood of encountering collagen layers and thus minimizing the bouncing effect.

From a mathematical point of view, the underestimation arises from a different perspective. Rather than adjusting the stiffness of the model, which remains constant, the observed phenomenon can be explained by changes in the reference configuration of the arterial segments. When subjected to higher pressures, the segments exhibit plasticity and fail to immediately return to their original reference configuration ( $l_0$ ,  $w_0$ , and  $h_0$ ). This deviation from the reference configuration needs a (re)estimation of these parameters to capture the behavior of the arterial segments under the new pressure conditions. In summary, while from a biological perspective the focus is on altering stiffness to explain the observed phenomena, from a mathematical one, the adjustment of the configuration parameters to account for the changes in arterial behavior is done.

The active pressure-stiffness curve (Figure 9B) demonstrates elevated arterial stiffness levels at lower mean pressures (80, 100 mmHg) in contrast to those observed under KR (Figure 9A) and DEANO (Figure 9C) conditions. This distinction is further evident in the corresponding diameter measurements, where exposure to PE (Figure 9E) yielded smaller diameters relative to those observed under KR (Figure 9D) and DEANO (Figure 9F) conditions. Consequently, this phenomenon leads to an augmented arterial stiffness, indicative of an enhanced buffering capacity and concomitant

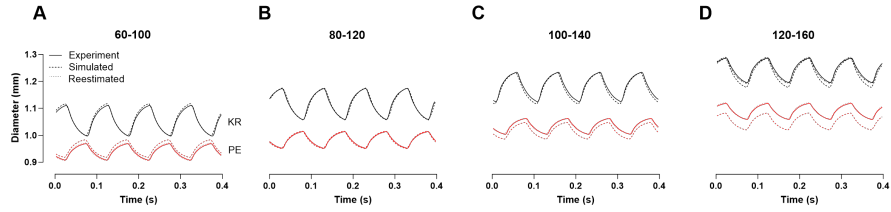


**Fig. 8:** Pressure steps under Krebs-Ringer and PE of one aortic segment

elevation in vascular tone. However, as mean pressures increase, the recruitment of collagen emerges as the predominant load-bearing component within the aortic wall. The absence of stiffer collagen fibers within our current model results in an underestimation of stiffness values at highest pressure (Figure 9A, 9B, 9C).

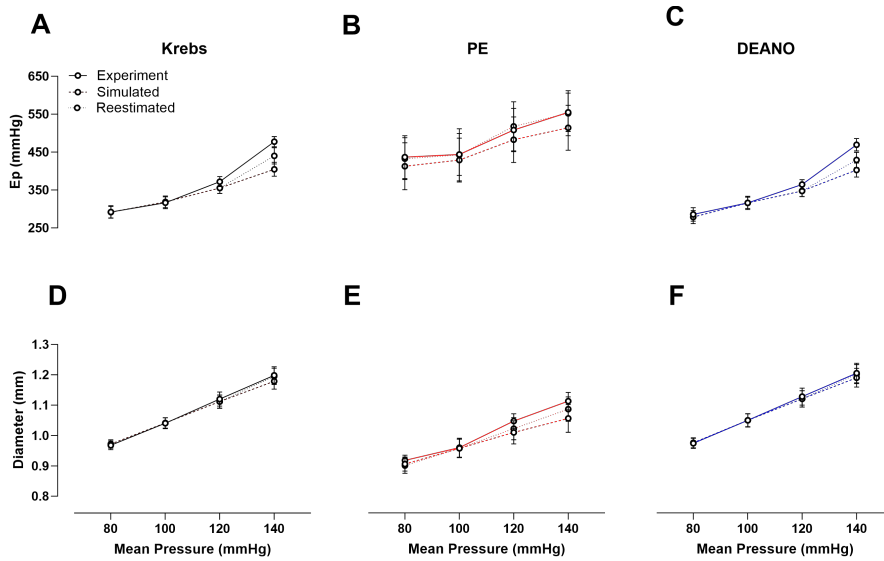


**Fig. 9:** Diastolic diameter and Peterson modulus for KR, PE and DEANO under different pressure steps

## 4 Discussion

In this study, we have introduced a mathematical framework capable of capturing both vasoconstriction and vasodilation, enabling the understanding of the mechanical behavior of arterial segments and the contribution of SMCs to arterial stiffness. This model was calibrated using isometric data to simulate the action of molecules on SMCs. Importantly, we not only established the model but also validated it against experimental data and explored two distinct scenarios to evaluate the impact of the

active contribution of SMCs on arterial mechanics. Furthermore, the model was tested with different pressure conditions beyond those used for parameter estimation, demonstrating its capacity of representing the pressure-diameter relationship except some deviations observed at higher pressures.

One of the interests of the present study was to determine whether the contraction of SMCs directly affects vascular tone by regulating stiffness through the fibers or whether this regulation indirectly adjusts intrinsic stiffness, as indicated by changes in the Young modulus. Additionally, the investigation explored the extent of alterations in geometry, such as changes in diameter, influence biomechanical assessments. Taking a look at how the pre-stress and elastic modulus of the fibers change compared to the baseline conditions gives us more understanding about the regulation of vascular tone. For vasoconstrictors, we observed an increase in pre-stress, reflecting increased arterial tension and reduced compliance. Conversely, the response to DEANO exhibited a more subtle variation, with pre-stress showing variable changes, influenced by the complex interplay of vasodilation and previously vasoconstriction compensatory mechanisms. Similarly, the elastic modulus exhibited distinct trends: vasoconstrictors tended to increase vessel stiffness, while vasodilators often led to a decrease or maintenance of elasticity, highlighting the dynamic nature of vascular responses to vasoactive compounds. In addition to the observed changes in pre-stress and elastic modulus of the active fibers, it is remarkable that the parameters associated with the passive component of the arterial wall, such as Young's modulus and thickness, exhibited minimal variation across conditions. The fact that there was no notable change, suggests that alterations in arterial mechanics primarily stem from the active component governed by SMC activity rather than intrinsic vessel properties. The Young's modulus staying comparatively stable indicates that the intrinsic stiffness of the vessel, represented by the passive component, remains largely unchanged. Instead, the variations in the fiber parameters point towards the crucial role of SMCs in mediating vasoconstriction and dilation, with minimal contribution from changes in intrinsic stiffness.

The simulated arterial stiffness values demonstrated a consistent decrement at higher pressures across all examined conditions in comparison to experimental values, necessitating a re-estimation. This observed discrepancy may potentially stem from the inherent limitations of the current model, which does not account for the recruitment of stiffer collagen fibers situated in the adventitial layer. These fibers are known to be recruited in a pressure-dependent manner within the aorta. Consequently, the model's omission of collagen loading contributes to an underestimation of stiffness values at highest pressures.

Overall, our work introduces a mathematical model to explore arterial mechanics, shedding light on the roles of SMCs. Moving forward, future research could focus on refining and validating the model to better capture the complex dynamics of arterial mechanics. This includes addressing limitations such as the lack of consideration for collagen loading, which may influence parameter estimation accuracy, particularly at higher pressures. As future work we would like to incorporate a more sophisticated model with a realistic geometry that also accounts for the contact between the aortic segment and the hooks, providing a more comprehensive understanding of vascular

mechanics and interactions. Moreover, the application of the model to *in vivo* data holds promising prospects for advancing our understanding of vascular physiology and guiding the development of further experiments. By integrating experimental findings and clinical data, the model can contribute to more accurate predictions of vascular behavior under physiological and pathological conditions.

## Acknowledgments

This work was funded by the INSPIRE European Training Network [49], through the EU Horizon 2020 Research and Innovation programme, under the Marie Skłodowska-Curie GA 858070.

## Author contributions

CW collected the data. CW and PJG assisted the data analysis from a biological viewpoint. SC developed the mathematical model, its implementation and the parameter estimation. MV, MF and DL contributed to mathematical model and parameter estimation definition. All authors contributed to the manuscript. CW and SC prepared the figures and the result analysis and post-processing.

## Declarations

**Competing interests.** The authors declare that they have no conflict of interest.

**Ethical approval.** The research conducted adhered to the standards outlined in the Guide for the Care and Use of Laboratory Animals, as issued by the US National Institutes of Health (NIH Publication No. 85-23, revised 1996), and all experimental procedures were in compliance with Directive 2010/63/EU of The European Parliament and The Council regarding the protection of animals used for scientific purposes. Furthermore, per the Belgium Royal Decree of May 2013, harvesting of organs for *ex vivo* analysis is not considered an animal experiment and therefore is exempt from ethical approval.

## Appendix A Experimental data

We have used *isometric data* gathered from 9 aortic segments that have been contracted with PE by adding cumulative concentrations and after dilated with DEANO with a similar protocol.

Regarding the *ROTSAC experiments*, we have used data from other 15 segments divided in four sets of five, two, two and six segments, respectively. The ROTSA data are presented in Table A1.

Pressures (mmHg)	Sets	KR	PE	DEANO
60 - 100	Set 4: 6 segments	✓	✓	✓
80 - 120	Set 1: 5 segments	✓	✓	
	Set 2: 2 segments	✓		
	Set 3: 2 segments	✓		
	Set 4: 6 segments	✓	✓	✓
100 - 140	Set 4: 6 segments	✓	✓	✓
120 - 160	Set 4: 6 segments	✓	✓	✓

**Table A1:** ROTsAC data of 15 aortic segments where KR stands for Krebs-Ringer; PE is the vasoconstrictor; DEANO is the vasodilator

## Appendix B Ogden's constitutive law

The simplest hyperelastic material model is the Saint-Venant-Kirchhoff model, which is just an extension of the geometrically linear elastic material model to the geometrically nonlinear regime.

The strain energy density function for the Saint-Venant-Kirchhoff model is

$$W(\mathbf{E}) = \frac{\lambda}{2} (\text{tr}(\mathbf{E}))^2 + \mu \text{tr}(\mathbf{E}^2). \quad (\text{B1})$$

Equation (B1) can be written in terms of the invariants of  $\mathbf{C}$  as

$$W = \left( \frac{\lambda}{8} + \frac{\mu}{4} \right) I_1^2 - \frac{\mu}{2} I_2 - \left( \frac{3\lambda}{4} + \frac{\mu}{2} \right) I_1 + \frac{9\lambda}{8} + \frac{3\mu}{4},$$

where  $\lambda$  is the first Lamé parameter and  $\mu$  is the shear modulus or the second Lamé parameter, given by

$$\lambda = \frac{\nu E}{(1 + \nu)(1 - 2\nu)}, \quad \mu = \frac{E}{2(1 + \nu)},$$

being  $E$  the Young modulus and  $\nu$  the Poisson's ratio.

The Saint-Venant Kirchhoff constitutive law is well-suited for materials with small deformations and linear stress-strain behavior. However, in scenarios involving large deformations and nonlinear stress-strain responses, such as those often encountered in biological tissues, this model may not offer accurate representations.

To capture more complex behaviors, the Ogden's constitutive law proves to be a better option for describing the passive component of the elastic medium. Ogden's model accommodates large deformations and nonlinear material responses, thereby providing a more accurate representation of the behavior seen in complex materials like rubbers, polymers, and biological tissues.

In terms of the invariants of  $\mathbf{C}$ , the Ogden's constitutive law [27] can be written as

$$W = c_1(I_1 - 3) + c_2(I_2 - 3) + a(I_3 - 1) - (c_1 + 2c_2 + a) \ln(I_3),$$

with  $c_1, c_2$  and  $a$  being the material parameters.

Interest lies in establishing a relation between the Ogden parameters and the Lamé parameters. The asymptotic behavior of the Ogden's law is examined as  $|\mathbf{E}| \rightarrow 0$ , aiming to identify it with the Saint-Venant-Kirchhoff law (B1). Upon conducting a limit development up to second order in  $\mathbf{e}$ , it can be demonstrated (refer to the detailed computation in Refs. [50, 51]).

$$\begin{cases} 2c_1 + 2c_2 = \mu, \\ c_2 + a = \frac{\lambda}{4}, \\ \lambda + 2\mu = 2b, \\ b = 2c_1 + 4c_2 + 2a. \end{cases}$$

Usually  $c_2$  can be chosen such that  $c_2 = c_1/\kappa$ , with  $\kappa \in [2, 100]$ . After doing some algebra, it is possible to write

$$\begin{cases} c_1 = \frac{E}{4(1 + \nu)(1 + \frac{1}{\kappa})}, \\ c_2 = \frac{c_1}{\kappa}, \\ a = \frac{\nu E}{4(1 + \nu)(1 - 2\nu)} - \frac{c_1}{\kappa}. \end{cases}$$

## Appendix C Isometric tests

In this appendix, more detailed results of the estimation of the range of the pre-stress from the isometric data are presented. In Figure C1, the fitting of the measured forces to equation (12) is shown.

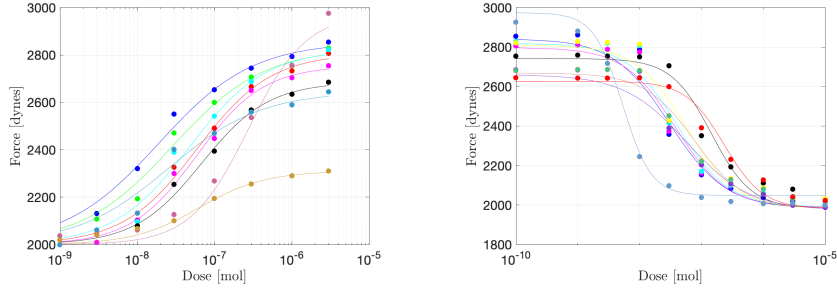


**Fig. C1:** Fitting of  $F_m$  to equation (12) for PE (left) and for DEANO (right) in semilog scale

The fitting of the data of the active pre-stress to equation (C2) is presented in Figure C2. Looking at the values at a concentration of  $2 \mu\text{M}$ , is possible to do an estimation of the range of  $k_0$ .

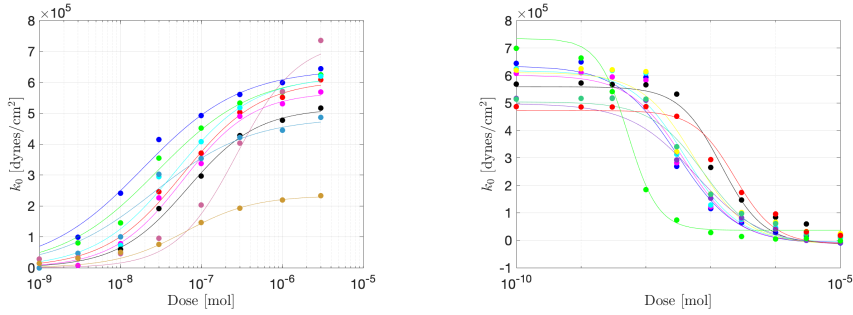


Fig. C2:  $k_0$  for PE (left) and for DEANO (right) in semilog scale

## Appendix D Optimization algorithm

To obtain the parameters for each aortic segment, a Control Random Search (CRS) algorithm is used for optimization [52]. The optimization problem is formulated in (8). A point  $\theta_{opt}$  is considered a global minimizer of  $J$  if  $J_{opt} = J(\theta_{opt}) \leq J(\theta)$  for all  $\theta \in \mathbf{W}$ .

CRS algorithms are better in high-dimensional problems compared to DIRECT algorithms. Unlike gradient-based methods, CRS algorithms do not use properties of the function being optimized. The only requirements are that  $J(\theta)$  can be computed for any  $\theta \in \mathbf{W}$ , and the explicit expression of the function being optimized must be known.

In each step of the algorithm,  $n + 1$  points are randomly chosen to create a simplex in  $n$ -dimensional space. One of these points becomes the pole, and the next trial point is determined by reflecting this pole relative to the centroid of the remaining points. This process generates primary trial points for exploration and secondary trial points for convergence, with the choice between them depending on the algorithm's success rate. If the success rate is below 50%, and a primary trial fails, a secondary point is selected for the next trial, maintaining a balanced approach between exploration and convergence during optimization.

In summary, the CRS algorithm is a heuristic, direct search method that begins by populating a set  $S$  with a large sample ( $N \gg n$ ) distributed uniformly over the search space  $\mathbf{W}$ . This sample is gradually contracted by replacing the worst point in  $S$  with a better trial point, forming a simplex with  $n + 1$  randomly chosen points from  $S$ . This process continues until a specified stopping condition is met.

The main issues with CRS are its lack of robustness in locating the global minimum and its decreased efficiency in convergence, particularly after reaching the region of the global minimum. To enhance the robustness and efficiency of CRS, Kaelo and Ali proposed variants such as CRS2, suggesting modifications to the trial point generation schemes [53]. Specifically, a CRS algorithm with local mutation for optimization is chosen [33].

In the original algorithm, if a trial point fails to improve upon the current worst point in the sample  $S$ , it is discarded, and a new simplex is formed using a new set of  $n + 1$  points from  $S$ .

In CRS with local mutation, the unsuccessful trial point is not discarded but used to obtain a second trial point. The point generation scheme is modified by introducing a local mutation technique. Whenever a trial point generated in CRS fails to replace the current worst point in  $S$ , local mutation generates a second trial point exploring the region around the current best point in  $S$  by reflecting the trial point through the current best point. This modification is utilized whenever a trial point fails to yield a function value that can replace the current worst point in  $S$ .

The introduction of local mutation has enhanced these algorithms' robustness in finding the global minimum and efficiency in reducing the number of function evaluations and CPU time. Additionally, the local mutation technique expedites convergence as soon as the region of the global minimizer is reached.

## References

- [1] Thomas, B., Sumam, K.S.: Blood flow in human arterial system-a review. *Procedia Technology* **24**, 339–346 (2016) <https://doi.org/10.1016/j.protcy.2016.05.045>
- [2] Shirwany, N.A., Zou, M.H.: Arterial stiffness: a brief review. *Acta Pharmacol Sin* **31**(10), 1267–1276 (2010) <https://doi.org/10.1038/aps.2010.123>
- [3] Vlachopoulos, C.: Prediction of cardiovascular events and all-cause mortality with arterial stiffness: a systematic review and meta-analysis. *J Am Coll Cardiol* **55**(12), 1318–1327 (2010) <https://doi.org/10.1016/j.jacc.2009.10.061>
- [4] Ghosh, A., Dharmarajan, A., Swain, P.K., Das, D., Verma, P., Tripathy, P.R.: Impact of cardiovascular factors on pulse wave velocity and total vascular resistance in different age group patients with cardiovascular disorders. *Curr Aging Sci* **11**(4), 261–268 (2019) <https://doi.org/10.2174/1874609812666190226151500>
- [5] Wang, M., Monticone, R.E., Lakatta, E.G.: Chapter 13 - the aging arterial wall. In: Kaeberlein, M.R., Martin, G.M. (eds.) *Handbook of the Biology of Aging* (Eighth Edition), pp. 359–389. Academic Press, San Diego, CA (2016). <https://doi.org/10.1016/B978-0-12-411596-5.00013-7>
- [6] Sahani, A.K., Shah, M.I., Radhakrishnan, R., Joseph, J., Sivaprakasam, M.: An imageless ultrasound device to measure local and regional arterial stiffness. *IEEE Trans Biomed Circuits Syst* **10**(1), 200–208 (2016) <https://doi.org/10.1109/TBCAS.2015.2394468>
- [7] Zhang, Y., Agnoletti, D., Xu, Y., Wang, J.G., Blacher, J., Safar, M.E.: Carotid-femoral pulse wave velocity in the elderly. *J Hypertens* **32**(8), 1572–1576 (2014) <https://doi.org/10.1097/HJH.000000000000187>
- [8] Sharif, S., Visseren, F.L.J., Spiering, W., Jong, P.A., Bots, M.L., Westerink, J.: Arterial stiffness as a risk factor for cardiovascular events and all-cause mortality



in people with type 2 diabetes. *Diabet Med* **36**(9), 1125–1132 (2019) <https://doi.org/10.1111/dme.13954>

- [9] Segers, P., Rietzschel, R. E, Chirinos, J.A.: How to measure arterial stiffness in humans. *Arteriosclerosis, Thrombosis, and Vascular Biology* **40**(5) (2020) <https://doi.org/10.1161/ATVBAHA.119.313132>
- [10] De Moudt, S., Hendrickx, J.O., Neutel, C., De Munck, D., Leloup, A., De Meyer, G.R.Y., al.: Progressive aortic stiffness in aging c57bl/6 mice displays altered contractile behaviour and extracellular matrix changes. *Communications Biology* **5**(1), 605 (2022) <https://doi.org/10.1038/s42003-022-03563-x>
- [11] Leloup, A.J.A., Van Hove, C.E., Kurdi, A., De Moudt, S., Martinet, W., De Meyer, G.R.Y., al.: A novel set-up for the ex vivo analysis of mechanical properties of mouse aortic segments stretched at physiological pressure and frequency. *J Physiol* **594**(21), 6105–6115 (2016) <https://doi.org/10.1113/JP272623>
- [12] Zulliger, M.A., Rachev, A., Stergiopoulos, N.: A constitutive formulation of arterial mechanics including vascular smooth muscle tone. *American Journal of Physiology-Heart and Circulatory Physiology* **287**(3), 1335–1344 (2004) <https://doi.org/10.1152/ajpheart.00094.2004>
- [13] Kerage, D., Brindley, D.N., Hemmings, D.G.: Review: novel insights into the regulation of vascular tone by sphingosine 1-phosphate. *Placenta* **35**, 86–92 (2014) <https://doi.org/10.1016/j.placenta.2013.12.006>
- [14] Sehgel, N.L., Zhu, Y., Sun, Z., Trzeciakowski, J.P., Hong, Z., Hunter, W.C., al.: Increased vascular smooth muscle cell stiffness: a novel mechanism for aortic stiffness in hypertension. *Am J Physiol Heart Circ Physiol* **305**(9), 1281–1287 (2013) <https://doi.org/10.1152/ajpheart.00232.2013>
- [15] Lacolley, P., Regnault, V., Segers, P., Laurent, S.: Vascular smooth muscle cells and arterial stiffening: Relevance in development, aging, and disease. *Physiol Rev* **97**(4), 1555–1617 (2017) <https://doi.org/10.1152/physrev.00003.2017>
- [16] Leloup, A.J.A., Van Hove, C.E., De Moudt, S., De Meyer, G.R.Y., De Keulenaer, G.W., Franssen, P.: Vascular smooth muscle cell contraction and relaxation in the isolated aorta: a critical regulator of large artery compliance. *Physiol Rep* **7**(4), 13934 (2019) <https://doi.org/10.14814/phy2.13934>
- [17] De Moudt, S., Hendrickx, J.O., Neutel, C., De Munck, D., Leloup, A., De Meyer, G.R.Y., Martinet, W., Franssen, P.: Aortic stiffness in l-name treated c57bl/6 mice displays a shift from early endothelial dysfunction to late-term vascular smooth muscle cell dysfunction. *Frontiers in Physiology* **13**, 874015 (2022) <https://doi.org/10.3389/fphys.2022.874015>

- [18] Bit, A., Suri, J.S., Ranjani, A.: Anatomy and Physiology of Blood Vessels. IOP Publishing, Bristol, United Kingdom (2020). <https://doi.org/10.1088/978-0-7503-2088-7ch1>
- [19] Coccarelli, A., Edwards, D.H., Aggarwal, A., Nithiarasu, P., Parthimos, D.: A multiscale active structural model of the arterial wall accounting for smooth muscle dynamics. *J R Soc Interface* **15**(139), 20170732 (2018) <https://doi.org/10.1098/rsif.2017.0732>
- [20] Liu, S.Q.: Influence of tensile strain on smooth muscle cell orientation in rat blood vessels. *Journal of Biomechanical Engineering* **120**(3), 313–320 (1998)
- [21] O’Connell, M.K., Murthy, S., Phan, S., Xu, C., Buchanan, J., Spilker, R., *et al.*: The three-dimensional micro- and nanostructure of the aortic medial lamellar unit measured using 3d confocal and electron microscopy imaging. *Matrix Biol* **27**, 171–181 (2008) <https://doi.org/10.008>
- [22] Murtada, S.-I., Holzapfel, G.A.: Investigating the role of smooth muscle cells in large elastic arteries: a finite element analysis. *J. Theor. Biol.* **358**, 1–10 (2014) <https://doi.org/10.1016/j.jtbi.2014.04.028>
- [23] Ambrosi, D., Pezzuto, S.: Active stress vs. active strain in mechanobiology: Constitutive issues. *Journal of Elasticity* **107**, 199–212 (2012) <https://doi.org/10.1007/s10659-011-9351-4>
- [24] Decoene, A., Martin, S., Vergnet, F.: A continuum active structure model for the interaction of cilia with a viscous fluid. *Journal of Applied Mathematics and Mechanics / Zeitschrift für Angewandte Mathematik und Mechanik* (2023) <https://doi.org/10.1002/zamm.202100534>
- [25] Lohr, M.J., Sugerman, G.P., Kakaletsis, S., Lejeune, E., Rausch, M.K.: An introduction to the ogden model in biomechanics: benefits, implementation tools and limitations. *Philos Trans A Math Phys Eng Sci* **380**, 20210365 (2022) <https://doi.org/10.1098/rsta.2021.0365>
- [26] Nedrelow, D.S., Townsend, J.M., Detamore, M.S.: The ogden model for hydrogels in tissue engineering: Modulus determination with compression to failure. *Journal of Biomechanics* **152**, 111592 (2023) <https://doi.org/10.1016/j.jbiomech.2023.111592>
- [27] Geymonat, G., Ciarlet, P.G.: Sur les lois de comportement en élasticité non linéaire compressible. *CR Acad. Sci. Paris Sér. II* **295**, 423–426 (1982)
- [28] Chapelle, D., Bathe, K.-J.: *The Finite Element Analysis of Shells: Fundamentals* vol. 1. Springer, ??? (2011)
- [29] Bischoff, M., Ramm, E.: Shear deformable shell elements for large strains and

- rotations. *International Journal for Numerical Methods in Engineering* **40**(23), 4427–4449 (1997)
- [30] Chapelle, D., Ferent, A., Bathe, K.J.: 3D-shell elements and their underlying mathematical model. *Math. Models Methods Appl. Sci.* **14**(1), 105–142 (2004) <https://doi.org/10.1142/S0218202504003179>
- [31] Libai, A., Simmonds, J.: *The Nonlinear Theory of Elastic Shells*. Cambridge University Press, Cambridge (2005)
- [32] Aletti, M., Gerbeau, J.-F., Lombardi, D.: Modeling autoregulation in three-dimensional simulations of retinal hemodynamics. *Modeling and Artificial Intelligence in Ophthalmology* **1**, 12 (2015) <https://doi.org/10.35119/maio.v1i1.17>
- [33] Kaelo, P., Ali, M.M.: Some variants of the controlled random search algorithm for global optimization. *Journal of Optimization Theory and Applications* **130**(2), 253–264 (2006) <https://doi.org/10.1007/s10957-006-9101-0>
- [34] Johnson, S.G.: *The Nlopt Nonlinear-optimization Package*, <http://github.com/stevengj/nlopt> (2014)
- [35] Yosibash, Z., Priel, E.: Artery active mechanical response: High order finite element implementation and investigation. *Computer Methods in Applied Mechanics and Engineering* **237-240**, 51–66 (2012) <https://doi.org/10.1016/j.cma.2012.05.001>
- [36] Lanir, Y.: Constitutive equations for fibrous connective tissues. *J Biomech* **16**, 1–12 (1983) [https://doi.org/10.1016/0021-9290\(83\)90041-6](https://doi.org/10.1016/0021-9290(83)90041-6)
- [37] Wuyts, F.L., Vanhuysse, V.J., Langewouters, G.J., Decraemer, W.F., Raman, E.R., Buyle, S.: Elastic properties of human aortas in relation to age and atherosclerosis: a structural model. *Phys Med Biol* **40**, 1577–1597 (1995) <https://doi.org/10.1088/0031-9155/40/10/002>
- [38] Dahl, S.L.M., Vaughn, M.E., Hu, J.J., Driessen, N.J.B., Baaijens, F.P.T., Humphrey, J.D.: A microstructurally motivated model of the mechanical behavior of tissue engineered blood vessels. *Ann Biomed Eng* **36**, 1782–1792 (2008) <https://doi.org/10.1007/s10439-008-9554-4>
- [39] Lokshin, O., Lanir, Y.: Micro and macro rheology of planar tissues. *Biomaterials* **30**, 3118–3127 (2009) <https://doi.org/10.1016/j.biomaterials.2009.02.039>
- [40] Hollander, Y., Durban, D., Lu, X., Kassab, G.S., Lanir, Y.: Experimentally validated microstructural 3d constitutive model of coronary arterial media. *J Biomech Eng* **133**, 031007 (2011) <https://doi.org/10.1115/1.4003324>

- [41] Rachev, A., Shazly, T.: A structure-based constitutive model of arterial tissue considering individual natural configurations of elastin and collagen. *J Mech Behav Biomed Mater* **90**, 61–72 (2019) <https://doi.org/10.1016/j.jmbbm.2018.09.047>
- [42] Gestrelus, S., Borgström, P.: A dynamic model of smooth muscle contraction. *Biophys J* **50**, 157–169 (1986) [https://doi.org/10.1016/S0006-3495\(86\)83448-8](https://doi.org/10.1016/S0006-3495(86)83448-8)
- [43] Yang, J., Clark, J.W., Bryan, R.M., Robertson, C.: The myogenic response in isolated rat cerebrovascular arteries: smooth muscle cell model. *Medical Engineering & Physics* **25**(8), 691–709 (2003) [https://doi.org/10.1016/s1350-4533\(03\)00100-0](https://doi.org/10.1016/s1350-4533(03)00100-0)
- [44] Stålhand, J., Klarbring, A., Holzapfel, G.A.: A mechanochemical 3d continuum model for smooth muscle contraction under finite strains. *J Theor Biol* **268**, 120–130 (2011) <https://doi.org/10.1016/j.jtbi.2010.10.013>
- [45] Clark, J.M., Glagov, S.: Transmural organization of the arterial media. the lamellar unit revisited. *Arteriosclerosis* **5**, 19–34 (1985) <https://doi.org/10.1161/01.ATV.5.1.19>
- [46] Wolinsky, H., Glagov, S.: A lamellar unit of aortic medial structure and function in mammals. *Circ Res* **20**, 99–111 (1967) <https://doi.org/10.1161/01.res.20.1.99>
- [47] Hansen, T.R., Dineen, D.X., Pullen, G.L.: Orientation of arterial smooth muscle and strength of contraction of aortic strips from doca-hypertensive rats. *Blood Vessels* **17**, 302–311 (1980) <https://doi.org/10.1159/000158261>
- [48] Stålhand, J., Klarbring, A., Holzapfel, G.A.: Smooth muscle contraction: mechanochemical formulation for homogeneous finite strains. *Progress in Biophysics and Molecular Biology* **96**(1-3), 465–481 (2008) <https://doi.org/10.1016/j.pbiomolbio.2007.07.025>
- [49] Guns, P.D., Guth, B.D., Braam, S., Kosmidis, G., Matsa, E., Delaunois, A., Gryshkova, V., Bernasconi, S., Knot, H.J., Shemesh, Y., Chen, A., Markert, M., Fernández, M.A., Lombardi, D., Grandmont, C., Cillero-Pastor, B., Heeren, R.M.A., Martinet, W., Woolard, J., Skinner, M., Segers, V.F.M., Franssen, C., Van Craenenbroeck, E.M., Volders, P.G.A., Pauwelyn, T., Braeken, D., Yanez, P., Correll, K., Yang, X., Prior, H., Kismihók, G., De Meyer, G.R.Y., Valentin, J.-P.: Inspire: A european training network to foster research and training in cardiovascular safety pharmacology. *Journal of Pharmacological and Toxicological Methods* **105**, 106889 (2020) <https://doi.org/10.1016/j.vascn.2020.106889>
- [50] Trabelsi, K.: On the modeling of thin plates in nonlinear elasticity. PhD thesis, Université Pierre et Marie Curie-Paris VI (2004)
- [51] Ciarlet, P.G.: Chapter 4: Hyperelasticity. In: Ciarlet, P.G. (ed.) *Mathematical Elasticity Volume I: Three-Dimensional Elasticity. Studies in Mathematics and Its Applications*, vol. 20, pp. 137–198 (1988). <https://doi.org/10.1016/>

S0168-2024(08)70061-4

- [52] Price, W.L.: A controlled random search procedure for global optimization. *Toward Global Optimization* 2, 71–84 (1978)
- [53] Price, W.L.: Global optimization by controlled random search. *Journal of Optimization Theory and Applications* **40**, 333–348 (1983)